3D Magnetic Textures with Mixed Topology: Unlocking the Tunable Hopf Index

Maria Azhar,[1] Sandra C. Shaju,[1] Ross Knapman,[1,2] Alessandro Pignedoli,[1] and Karin Everschor-Sitte[1]

[1] *Faculty of Physics and Center for Nanointegration Duisburg-Essen (CENIDE), University of Duisburg-Essen, 47057 Duisburg, Germany*

[2] *Institute of Mechanics, Faculty of Engineering, University of Duisburg-Essen, 45141 Essen, Germany*

Knots and links play a crucial role in understanding topology and discreteness in nature. In magnetic systems, twisted, knotted and braided vortex tubes manifest as Skyrmions, Hopfions, or screw dislocations. These complex textures are characterized by topologically non-trivial quantities, such as a Skyrmion number, a generalized Hopf index H, a Burgers vector (quantified by an integer ν), and linking numbers. In this work, we introduce a discrete geometric definition of H for periodic magnetic textures, which can be separated into contributions from the self-linking and inter-linking of flux tubes of the emergent magnetic field of non-coplanar textures. We show that fractional Hopfions or textures with non-integer values of H naturally arise and can be interpreted as states of "mixed topology" that are continuously transformable to one of the multiple possible topological sectors. Our findings demonstrate a solid physical foundation for the generalized Hopf index to take integer, non-integer, or specific fractional values, depending on the underlying topology of the flux tubes of the emergent magnetic field of the system.

I. INTRODUCTION

Knots, links, and braids are important across a wide range of scientific disciplines and are realisable in diverse physical platforms [1] such as water [2, 3], quantum gases [4], electromagnetic waves [5], DNA [6], superfluids [7], liquid crystals [8–11], laser light [12, 13], high energy physics [14], frustrated magnets [15, 16] and chiral magnets [17–22]. These phenomena are significant across length scales, from the smallest lengths in the early cosmology of the universe [23] to magnetic braids in the solar corona that store vast amounts of energy, making them several times hotter than the surface of the sun [24].

In magnetic materials, a multitude of topologically non-trivial textures has been realized [25], such as Skyrmions in 2D systems that can be readily manipulated with external fields and have potential in device applications [26–29]. In 3D systems, the addition of a third spatial dimension enriches the applications of topology by enabling knots, links and braids, to form textures [30–32] such as Hopfions [15, 33] or the recently predicted [21] and observed [22] screw dislocations. Also, 3D textures exhibit complex dynamics under applied drives [34–38], making them interesting for applications. Notably, the family of topological defects has been expanded to include textures where non-integer Hopf indices have been calculated [32, 39, 40].

Magnetic textures have typically been characterized based on the homotopy groups of spheres or mapping of the magnetization $\mathbf{m}$ from a base space to the target space S^2, where S^n denotes the surface of the unit sphere in $n+1$ dimensions. In the special case where $\mathbf{m}$ decays to a constant $\mathbf{m}_0$ at infinity, allowing a "one-point compactification", e.g. $\mathbb{R}^2 \to S^2$ or $\mathbb{R}^3 \to S^3$ for textures in 2D and 3D physical space respectively, the standard homotopy groups resulting in integer values of the Skyrmion number N_{sk} and Hopf index H are $\pi_2(S^2) = \mathbb{Z}$ and $\pi_3(S^2) = \mathbb{Z}$. Topological stability is then derived from the fact that knotted textures in a continuous field cannot be unwound without introducing singularities, violating the continuity of the field or modifying the base space.

In two-dimensional magnetic systems, it is common to describe certain textures using fractional topological charges—for example, assigning a Skyrmion number $N_{\text{sk}} = \pm 1/2$ to merons [11, 41–43]. While this assignment is not strictly justified by homotopy theory—and alternative classifications of merons using pairs of integers do exist [44]—it remains an immensely practical and physically meaningful convention. The $1/2$ charge reflects the partial coverage of the magnetization sphere S^2 and provides an intuitive quantification of a meron's contribution to dynamical quantities such as the gyrovector and emergent electrodynamics. In particular, it allows merons to be treated analogously to Skyrmions (i.e., textures with $N_{\text{sk}} = \pm 1$) in collective coordinate models, where the effective force and motion scale proportionally with N_{sk}. Thus, the fractional charge plays a central role in both understanding and modeling meron dynamics.

Despite the growing interest in complex 3D textures, an intuitive and broadly applicable framework for describing non-integer values of H, analogous to the use of fractional topological charges in 2D systems, has yet to be established.

In this work, we introduce such a framework for analytically determining generalized Hopf index values in 3D topological textures particularly in cases where one-point compactification is not possible—such as magnetic textures embedded in non-uniform physical backgrounds, including conical spiral [20, 45–47], vortex, or screw dislocation [21] configurations. To address this, we define a generalized non-integer Hopf index H, based on the structure and linking of flux tubes associated with the emergent magnetic field. The resulting linking numbers [48–52] serve as topological invariants that extend the classification of such textures beyond traditional integer-valued topological indices. We demonstrate that arbitrary non-integer values of the generalized Hopf in-

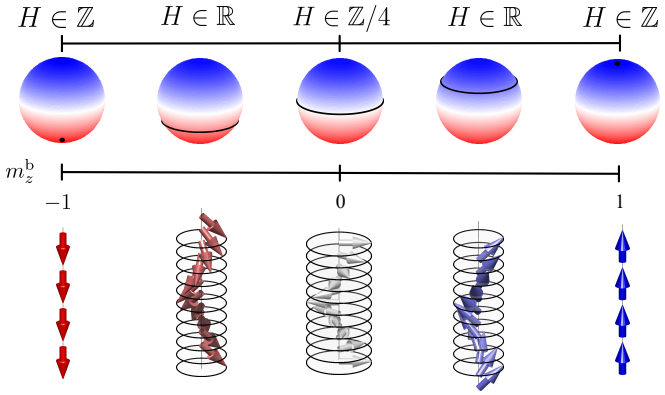

FIG. 1. The generalized Hopf index, H, can take arbitrary values when the z-component of the background magnetization m_z^{b} (lower panel) maps to an S^1 line within the target space S^2 of the magnetization vector $\mathbf{m}$ (upper panel). Here, the background magnetization is defined by $\lim_{|\mathbf{r}_\perp|\to\infty} \mathbf{m}(\mathbf{r})$, with $\mathbf{r}_\perp = (x, y)$ and its z-component determines the latitude of the line effectively partitioning the S^2 sphere into two topologically distinct subspaces.

dex naturally arise for magnetic structures whose far field or background magnetization is non-compactifiable, and maps to an S^1 line on the S^2 magnetization sphere (see Fig. 1), despite a discrete representation of the generalized Hopf index by a finite number of flux tubes.

Here we focus on magnetization textures which are periodic along a certain axis labelled as z. In this case, the base space changes from S^3 to $S^2 \times S^1$ [22, 40, 53–58] and as far field or background magnetization we consider $\lim_{|\mathbf{r}_\perp|\to\infty} \mathbf{m}(\mathbf{r})$, with $\mathbf{r}_\perp = (x, y)$. The corresponding z-component of this far field m_z^b then divides the S^2 target space into two subspaces [59, 60] (indicated by the black line in Fig. 1). Linking numbers must be introduced for the top and bottom target subspaces individually (self-linking), as well as additional inter-linking numbers involving both subspaces. Here the linking numbers and the generalized Hopf index are calculated per period [61]. Furthermore, H is maintained as a measure of the generalized Hopf index *relative* to the unlinked state that has the same configuration at the boundary of the volume [61, 62].

Upon continuously tuning the background magnetisation m_z^{b} up or down, the generalized Hopf index is continuously modified without changing the linking numbers. Once the background magnetization collapses to a single point on S^2, the generalized Hopf index becomes integer-valued and equivalent to the conventional Hopf index defined by $\pi_3(S^2) = \mathbb{Z}$. We illustrate this finding with a plethora of examples of smooth topological magnetic structures. This work provides a unique framework to characterize, explain and classify the wealth of 3D topological textures in magnetism.

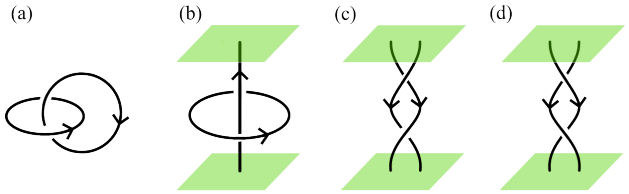

FIG. 2. Here, we illustrate examples of two linked field lines. The green surfaces indicate periodic boundary conditions along the vertical axis. In panel (a), the field lines form closed, linked loops. Panel (b) shows a loop threaded by a vertical line. Panels (c) and (d) display vertically braided lines. The linking number of the field lines is +1 in scenarios (a-c), and −1 in (d) according to Eq. (2).

A. Hopf index in terms of flux tubes

The generalized Hopf index, or the helicity integral H, characterizes the topological properties of the field lines in a vector field $\mathbf{F}$, such as their linking number [61, 63–66]. Field lines of $\mathbf{F}$ are oriented curves that are tangent at every point to the direction of $\mathbf{F}$. The generalized Hopf index can be written in a discrete geometric form for flux tubes [67], i.e. bundles of field lines as [52, 64, 68, 69],

$$H = \sum_{i=1}^{N_\Phi} L_{ii}\Phi_i^2 + \sum_{\substack{i=1 \\ j\neq i}}^{N_\Phi} L_{ij}\Phi_i\Phi_j. \tag{1}$$

Here, the vector field $\mathbf{F}$ has been decomposed into N_Φ flux tubes. Φ_i is the (positive definite) flux of the flux tube labelled by the index i, i.e. $\Phi_i = |\int_{\mathbf{a}_i} \mathrm{d}\mathbf{a} \cdot \mathbf{F}|$, where the integration is over a cross-sectional area $\mathbf{a}_i$ of the flux tube. The linking numbers L_{ii} and L_{ij} are respectively the oriented self-linking of the flux tube i and the oriented inter-linking of flux tubes i and j. L_{ij} (for $i \neq j$) is computed using the Gauss linkage formula,

$$L_{ij} = \frac{1}{4\pi} \oint_{C_i} \oint_{C_j} \frac{\mathbf{r}_i - \mathbf{r}_j}{|(\mathbf{r}_i - \mathbf{r}_j)|^3} \cdot (\mathrm{d}\mathbf{r}_i \times \mathrm{d}\mathbf{r}_j), \tag{2}$$

using the contour C_i (C_j) following an arbitrarily chosen field line belonging to flux tube i (j) [70]. L_{ii} is calculated analogously using the contours of two non-coinciding field lines within the same tube i. The sign of the linking numbers L_{ii} and L_{ij} are determined by the direction of the pairs of contours as depicted in Fig. 2 [71], with further examples shown in Sec. I of the Supplementary Material.

Equation (1) decomposes H into two contributions that, while geometrically distinct, are topologically equivalent. It also indicates that when the fluxes are non-integer, H can assume non-integer values. Moreover, H is conserved under flux-preserving continuous deformations of $\mathbf{F}$.

A significant advantage of Eq. (1) is its intuitiveness and ease of analytical calculation in comparison with the mathematically equivalent well-known Whitehead integral formula [64, 72] $H = \int \mathrm{d}^3 r\, \mathbf{F} \cdot \mathbf{A}$ with $\mathbf{F} = \boldsymbol{\nabla} \times \mathbf{A}$.

The latter can only be analytically computed for a limited set of specific ansatzes [73, 74], and its numerical computation requires careful implementation [75].

B. Hopf index in magnetism

In magnetism, the vector field $\mathbf{F}$ for which the Hopf index H is typically calculated is the emergent magnetic field defined by [76, 77]

$$F^k = \frac{1}{8\pi}\epsilon^{ijk}\mathbf{m}\cdot(\partial_i\mathbf{m}\times\partial_j\mathbf{m}), \tag{3}$$

where ϵ^{ijk} is the Levi-Civita symbol, $i,j,k\in\{x,y,z\}$ and the normalized vector field $\mathbf{m}$ represents the magnetic texture.

To calculate the generalized Hopf index for the emergent magnetic field, Eq. (1) can generally be applied after the division of field lines of $\mathbf{F}$ into flux tubes. Each flux tube contributes a flux $\Phi_i = |N_{\mathrm{sk},i}|$, where $N_{\mathrm{sk},i} = \int_{\mathbf{a}_i} \mathrm{d}\mathbf{a}\cdot\mathbf{F}$ is the Skyrmion number calculated for the cross-sectional area $\mathbf{a}_i$ of the flux tube i of the emergent magnetic field [78] Importantly, a flux tube can be arbitrarily decomposed into its constituent parts without affecting the validity of Eq. (1), as we exemplify explicitly for a Skyrmion and a Hopfion in Sec. II of the Supplementary Material.

In magnetism, it is common to consider the preimages of magnetization $\mathbf{m}$, which are lines of constant $\mathbf{m}$, to obtain information about the Hopf index. The preimages of $\mathbf{m}$ coincide at a local level with the field lines of $\mathbf{F}$ only if $\boldsymbol{\nabla}\cdot\mathbf{F}=0$ [79], i.e. in the absence of Bloch points. In contrast to preimages, however, only the field lines of $\mathbf{F}$ possess a distinct direction, which is indispensable for unambiguously determining the sign of the linking number and hence the proper calculation of the Hopf index H, as emphasized by the sketches shown in Fig. 2.

II. ANALYTICAL RESULTS

As a central result, we demonstrate that the generalized Hopf index is a continuously tunable function of the total magnetization of the background. Notably, the value of H can be adjusted through the application of external magnetic fields.

For periodic magnetic structures along z with background magnetization characterized by m_z^{b} or those with a uniform background $|m_z^{\mathrm{b}}|=1$, we can express the generalized Hopf index H and the skyrmion number N_{sk} respectively as

$$H = \begin{cases} \in\mathbb{Z} & \text{if } |m_z^{\mathrm{b}}|=1,\\ \in\mathbb{Z}/4 & \text{if } m_z^{\mathrm{b}}=0,\\ \in\mathbb{R} & \text{otherwise} \end{cases} \tag{4}$$

which can be proven with the help of Eq. (1), and

$$N_{\mathrm{sk}} = \begin{cases} \in\mathbb{Z} & \text{if } |m_z^{\mathrm{b}}|=1,\\ \in\mathbb{Z}/2 & \text{if } m_z^{\mathrm{b}}=0,\\ \in\mathbb{R} & \text{otherwise.} \end{cases} \tag{5}$$

For magnetic textures embedded in a ferromagnet ($|m_z^b|=1$), the far field maps to a single point on the S^2 sphere. In this case, the physical space can be compactified enforcing integer-valued N_{sk} and H, with the latter coinciding with the Hopf index.

When the far field is not ferromagnetic and the background maps to an S^1 line on the S^2 sphere (see Fig. 1), such as for helimagnets [20, 21, 45–47], H is not guaranteed to be an integer [80]. Instead, H is a real number and depends on the total magnetization of the background m_z^{b}. In this case, the noncollinear background splits the magnetization S^2 target space into two topologically distinct subspaces. These subspaces map from specific regions in physical space (where flux tubes reside), enabling an unambiguous assignment of each flux tube to either of the two subspaces. This necessitates the introduction of the concept of self-linking numbers for flux tubes belonging either to the top or bottom subspaces, and the inter-linking number for two flux tubes belonging to different subspaces.

A special case arises for magnetic textures with a far field described by $m_z^b=0$, where the S^2 sphere is split into half. In this case, the Skyrmion number of individual flux tubes is restricted to assume integer or half-integer values, i.e. $N_{\mathrm{sk},i}\in\mathbb{Z}/2$ and $N_{\mathrm{sk}}\in\mathbb{Z}/2$. Since for periodic structures, it is always possible to find a decomposition of field lines into flux tubes where all linking numbers are integers, it follows from Eq. (1) that H generally takes fractional values $H\in\mathbb{Z}/4$.

To demonstrate the versatility of Eqs. (1) and (4), we now discuss specific examples.

Magnetic textures for which the flux tubes are not linked have a Hopf index of zero. Examples of this are magnetic structures translationally invariant along the z-direction, such as vertical Skyrmion tubes (see Fig. 3(a)) or meron tubes (see Fig. 4(a)).

In Sec. II A, II B and Sec. II C we discuss textures consisting of either a single flux tube, or multiple flux tubes spatially separated by the isosurface defined by $m_z=m_z^{\mathrm{b}}$, categorized according to Eq. (4). We summarize the calculations of key topological properties, including the Hopf index of the corresponding magnetic textures in Tables I and II [81].

A. 3D textures in ferromagnetic background $|m_z^{\mathrm{b}}|=1$

Figure 3 shows topological field configurations with a ferromagnetic background. Here the vector field can be decomposed into flux tubes which each have $\Phi=1$.

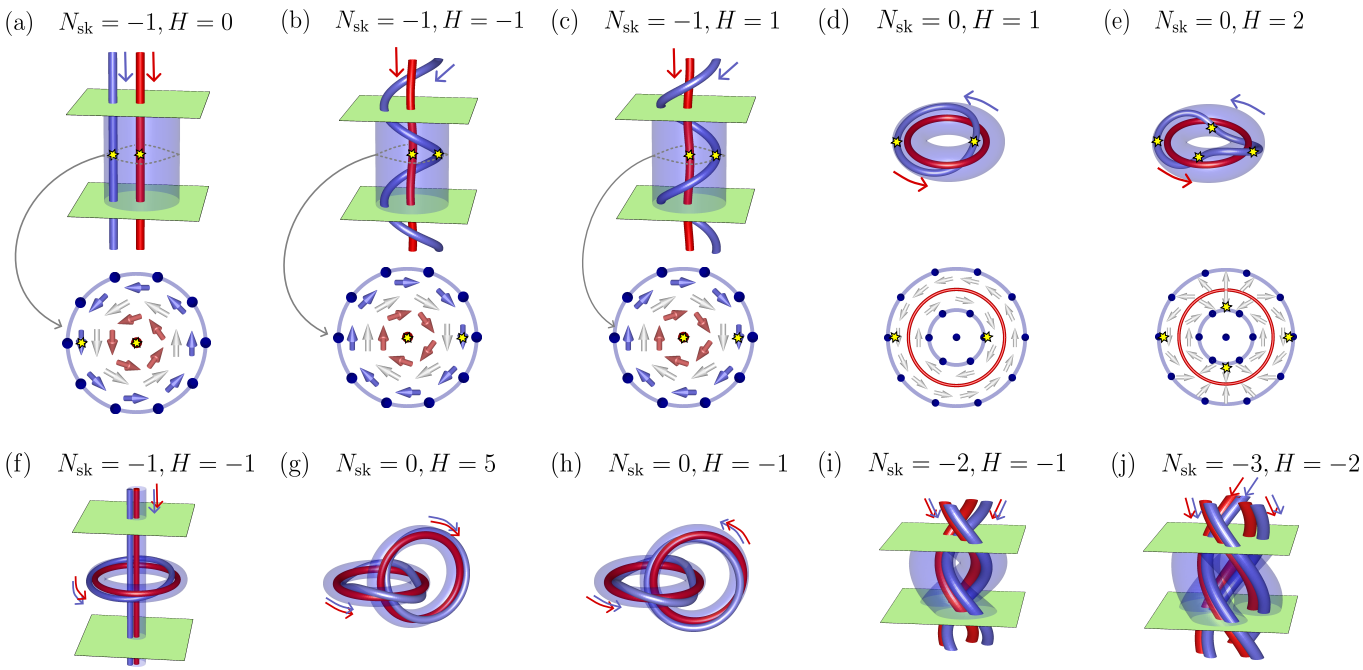

FIG. 3. **Illustrative examples applying Eq. (1) to spin textures with a ferromagnetic background ($m_z^{\rm b}=1$):** All panels show spin textures composed of $\Phi=1$ flux tubes enclosed by the transparent blue isosurface where $m_z=1$. For each flux tube two field lines of $\mathbf{F}$ are highlighted, which correspond to the preimages of $\mathbf{m}=(0,0,-1)$ and $\mathbf{m}=(0,-0.87,0.50)$, respectively accompanied by thin arrows showing the direction of the field line. The green planes represent the periodic boundary conditions along the vertical axis. The middle row shows cross-sections of the 3D structures depicted in a)–e) with the thick arrows indicating the spin direction. Yellow stars indicate the point of intersection of the field lines and the central horizontal plane. The colour code corresponds to the S^2 sphere shown in Fig. 1. (a) A vertical Skyrmion string without self-linking, (b,c) vertical Skyrmion strings with self-linking ±1, (d) a Hopfion, (e) a Hopfion with self-linking 2, (f) a Hopfion encircling a vertical Skyrmion tube, (g,h) interlinked Hopfions, (i,j) braided Skyrmion tubes.

We further show two field lines for each flux tube, whose linking we determine according to the convention in Fig. 2. We then compute the corresponding Hopf indices based on Eq. (1). When there is only a single flux tube, as in Fig. 3 (a-e), then the equation for the Hopf index reduces to $H=L_{11}\Phi_1^2=L_{11}$. For the examples shown in Fig. 3 (f-j), the interlinking between pairs of tubes also needs to be considered. Note that each Skyrmion tube that is inserted inside a Hopfion changes the Hopf index by $L_{ii}+2$ where L_{ii} is the self-linking of the Skyrmion. The calculation of the Hopf indices is summarized in Table I.

The examples shown indicate that the classification in terms of linking numbers provides a more thorough description of magnetic textures than classifying them by H and $N_{\rm sk}$ only. For example, the two different spin textures are shown in Fig. 3(b) and (f) have the same topological indices but different linking numbers.

B. 3D textures with $|m_z^{\rm b}|=0$:

When the far field of the texture is an S^1 line, the S^2 sphere is naturally split into two subspaces. The corresponding magnetic textures can be geometrically decomposed into their fractional components, that are flux tubes of $\mathbf{F}$. For $|m_z^{\rm b}|=0$, a distribution of space into flux tubes can be made such that all flux tubes carry a flux of $\Phi=1/2$. Examples of such textures are illustrated in Fig. 4.

To construct an S^1 background, we describe the magnetization using the angular parameterization

$$\mathbf{m}=(\cos\phi\sin\theta,\sin\phi\sin\theta,\cos\theta). \tag{6}$$

In the far field, the spins can either rotate along the z-axis (as a helical spiral $\phi=qz$ with ferromagnetic ordering within each xy-plane, see Fig. 4(b,c)) or assume an in-plane vorticity, ($\phi=\nu\chi$, where ν is an integer and $\chi=\arctan(y/x)$, while being invariant along the z-direction, see Fig. 4(a)), or a combination of both a spiral and a vortex state, which is a screw dislocation [21] ($\phi=\nu\chi+qz$, where here ν is the integer quantising the Burgers vector, see Fig. 4(d-g)). In the following sections, we describe these textures in detail and apply Eq. (1) to them.

	N_{sk}	Self-linking	H
(a)	-1	$L_{11} = 0$	0
(b)	-1	$L_{11} = -1$	-1
(c)	-1	$L_{11} = 1$	1
(d)	0	$L_{11} = 1$	1
(e)	0	$L_{11} = 2$	2

	N_{sk}	Self-linking	Inter-linking	H
(f)	-1	$L_{11} = 1$ $L_{22} = 0$	$L_{12} = -1$	$1 + 0 + 2 \times (-1) = -1$
(g)	0	$L_{11} = 2$ $L_{22} = 1$	$L_{12} = 1$	$2 + 1 + 2 \times 1 = 5$
(h)	0	$L_{11} = 2$ $L_{22} = -1$	$L_{12} = -1$	$2 - 1 + 2 \times (-1) = -1$
(i)	-2	$L_{11} = 0$ $L_{22} = 0$	$L_{12} = -\frac{1}{2}$	$2 \times \left(-\frac{1}{2}\right) = -1$
(j)	-3	$L_{11} = 0$ $L_{22} = 0$ $L_{33} = 0$	$L_{12} = -\frac{1}{3}$ $L_{23} = -\frac{1}{3}$ $L_{31} = -\frac{1}{3}$	$2 \times \left(-\frac{1}{3}\right) + 2 \times \left(-\frac{1}{3}\right)$ $+2 \times \left(-\frac{1}{3}\right) = -2$

TABLE I. Hopf index calculation for the spin textures shown in Fig. 3. The value of all fluxes is $\Phi_i = 1$.

(a) Meron

A meron is a texture characterized by a vortex-like far field ($\phi = \chi$), and a single vertical flux tube at its core, as illustrated in Fig. 4(a). The magnetization maps to half of the S^2 sphere, resulting in a flux value of $\Phi = 1/2$. The flux tube shown is aligned along the z-axis, with all field lines of $\boldsymbol{F}$ running parallel to the z-axis, hence $N_{\rm sk} = -1/2$. Since the flux tube of the magnetic texture has no self-linking, the generalized Hopf index is zero, as discussed above.

(b) Skyrmion in spiral background

Fig. 4(b) shows a Skyrmion with $N_{\rm sk} = -1$ embedded in a spiral background [45]. The Skyrmion string is aligned parallel to the z-axis, which is the direction of the wavevector of the spiral. Each xy-plane contains a vortex and an antivortex with opposite core magnetization m_z; hence, each individual xy-plane constitutes a bimeron configuration [82, 83]. Analysing the linkage of the field lines of $\mathbf{F}$, the vortex tube has a self-linking number $L_{11} = 0$, while the antivortex tube has $L_{22} = 2$. The inter-linking between these two tubes is $L_{12} = 1$. Thus, we obtain a generalized Hopf index of $H = L_{11}\Phi_1^2 + L_{22}\Phi_2^2 + 2L_{12}\Phi_1\Phi_2 = 1$.

(c) Heliknoton

A Heliknoton [20] can be interpreted as a Hopfion embedded within a spiral background, see Fig. 4(c). It consists of two flux tubes mapping to the upper and lower half of the S^2 sphere respectively, each with a flux value of $\Phi_1 = \Phi_2 = 1/2$ and linking numbers $L_{11} = L_{22} = L_{12} = 1$. The Skyrmion number in any cross-sectional plane is given by $N_{\rm sk} = 0$ and the generalized Hopf index evaluates to $H = 1$.

(d-e) Vortex and antivortex tubes with self-linking

Figure 4(d) and (e) show special types of screw dislocations composed of a single flux tube with self-linking and a Burgers integer of $|\nu| = 1$[84]. In (d) and (e) the cross-section is a vortex ($\nu = 1$) and an anti-vortex ($\nu = -1$), respectively.

For such single flux tube screw dislocations with Burgers integer ν the flux is $\Phi = |\nu/2|$ and the self-linking is $L_{11} = -1/\nu$. The Skyrmion charge is given by $N_{\rm sk} = p\nu/2$, where p denotes the core polarity (the sign of m_z at the core) and the generalized Hopf index is, $H = L_{11}\Phi_1^2 = -\nu/4$.

(f) Twiston

Figure 4(f) shows a special type of screw dislocation with $\nu = 1$ which we denote as "Twiston" in the following [85]. It is composed of two flux tubes: at the centre of the structure is a vertical meron tube with parameters $\Phi_1 = 1/2$, $L_{11} = 0$, and polarity p. Surrounding this is a meron-torus with $\Phi_2 = 1/2$, $L_{22} = 1$, and opposite polarity $-p$. There is inter-linking between these tubes, with a linking number $L_{12} = 1$. The Skyrmion number for each cross-section is $N_{\rm sk} = p/2$ and the generalized Hopf index H for this configuration is $H = 3/4$. A Twiston with $p = -1$ is illustrated in Fig. 4(f).

(g) Screw dislocation with $\nu = 2$

The screw dislocation illustrated in Fig. 4(g) consists of two flux tubes that do not have any self-linking, i.e., $L_{11} = L_{22} = 0$. Each flux tube has a flux $\Phi_1 = \Phi_2 = 1/2$, and their inter-linking is $L_{12} = 1$. The Skyrmion charge in the xy-plane for this configuration is $N_{\rm sk} = 0$. The generalized Hopf index is $H = 1/2$.

(h) Screw dislocation with $\nu = 3$

Figure 4(h) shows a screw dislocation with $\nu = 3$, which consists of three meron flux tubes each with flux

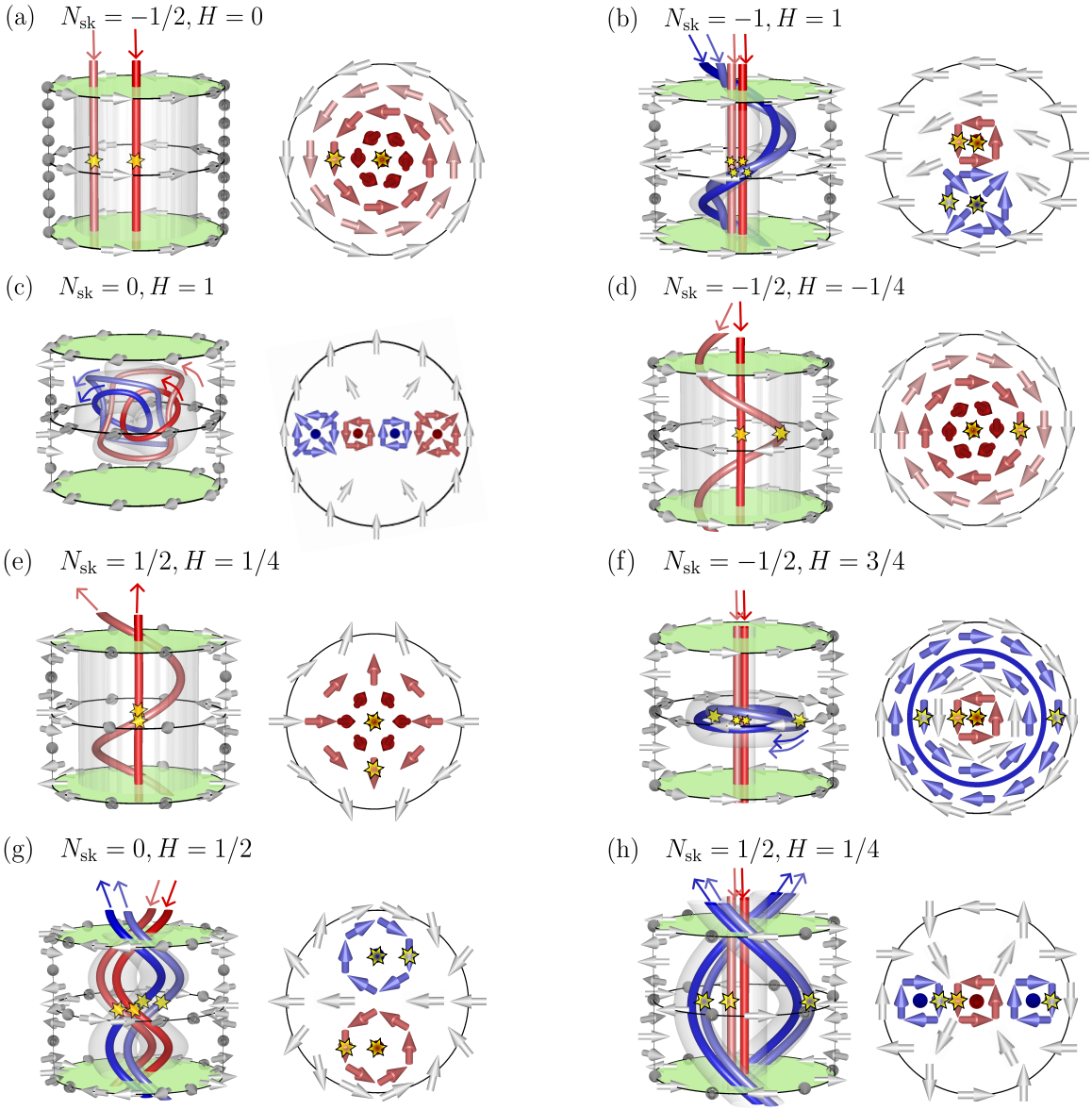

FIG. 4. **Illustrative examples applying Eq. (1) to spin textures with a spiral background ($m_z^{\rm b} = 0$):** All panels show spin textures composed of $\Phi = 1/2$ flux tubes enclosed by the transparent white isosurface where $m_z = 0$. For each flux tube, two field lines of $\mathbf{F}$ are highlighted, which correspond to the preimages of $\mathbf{m} = (0, 0, \pm 1)$ and $\mathbf{m} = (0, -0.87, \pm 0.50)$, respectively accompanied by thin arrows showing the direction of the field line. The green planes represent the periodic boundary conditions along the vertical axis. The second panel shows cross-sections of the 3D structures through the middle plane, with yellow stars indicating the point of intersection of the field lines and this plane, and thick arrows indicating the direction of $\mathbf{m}$. The colour code corresponds to the S^2 sphere shown in Fig. 1. We depict (a) a meron (b) Skyrmion and (c) Heliknoton, in a spiral background. (d-e) meron with self-linking (f) Twiston (a vertical meron tube surrounded by a self-linked meron torus) (g) two braided meron tubes (h) three braided meron tubes.

$\Phi_1 = \Phi_2 = \Phi_3 = 1/2$. None of the flux tubes have self-linking, i.e., $L_{11} = L_{22} = L_{33} = 0$, however their inter-linking numbers are $L_{23} = -1/2$ and $L_{12} = L_{13} = 1/2$. The Skyrmion charge in the xy-plane for this configuration, contributed by the three merons, is $N_{\rm sk} = 1/2$. The generalized Hopf index is $H = 1/4$.

C. 3D textures with $0 < |m_z^{\rm b}| < 1$

For magnetic textures where the background magnetization is neither along the z direction nor in the xy-plane, the results obtained in Sec. II B can be generalized.

For a background magnetization with $0 < |m_z^{\rm b}| < 1$ the S^1 line on the S^2 sphere shifts in latitude (see Fig. 1). This enables the partitioning of physical space into flux

	Burgers vector, ν	$N_{\rm sk}$	Both points at $m_z < m_z^{\rm b}$		Both points at $m_z > m_z^{\rm b}$		One at $m_z < m_z^{\rm b}$ and one at $m_z > m_z^{\rm b}$	H
			L_{11}	Φ_1	L_{22}	Φ_2	L_{12}	
(a)	-	$-\frac{1+m_z^{\rm b}}{2}$	0	$\frac{1+m_z^{\rm b}}{2}$				0
(b)	0	-1	0	$\frac{1+m_z^{\rm b}}{2}$	2	$\frac{1-m_z^{\rm b}}{2}$	1	$1-m_z^{\rm b}$
(c)	0	0	1	$\frac{1+m_z^{\rm b}}{2}$	1	$\frac{1-m_z^{\rm b}}{2}$	1	1
(d)	1	$-\frac{1+m_z^{\rm b}}{2}$	-1	$\frac{1+m_z^{\rm b}}{2}$				$-\frac{1}{4}-\frac{m_z^{\rm b}}{2}-\frac{(m_z^{\rm b})^2}{4}$
(e)	-1	$\frac{1+m_z^{\rm b}}{2}$	1	$\frac{1+m_z^{\rm b}}{2}$				$\frac{1}{4}+\frac{m_z^{\rm b}}{2}+\frac{(m_z^{\rm b})^2}{4}$
(f)	1	$-\frac{1+m_z^{\rm b}}{2}$	0	$\frac{1+m_z^{\rm b}}{2}$	1	$\frac{1-m_z^{\rm b}}{2}$	1	$\frac{3}{4}-\frac{m_z^{\rm b}}{2}-\frac{(m_z^{\rm b})^2}{4}$
(g)	2	$-m_z^{\rm b}$	0	$\frac{1+m_z^{\rm b}}{2}$	0	$\frac{1-m_z^{\rm b}}{2}$	1	$\frac{1}{2}-\frac{(m_z^{\rm b})^2}{2}$
(h)	3	$\frac{1-3m_z^{\rm b}}{2}$	$L_{11}=0$	$\frac{1+m_z^{\rm b}}{2}$	$L_{22}=0$ $L_{33}=0$ $L_{23}=-1/2$	$\frac{1-m_z^{\rm b}}{2}$	$L_{12}=1/2$ $L_{13}=1/2$	$\frac{1}{4}+\frac{m_z^{\rm b}}{2}-\frac{3(m_z^{\rm b})^2}{4}$

TABLE II. Calculation of the generalized Hopf index for the textures shown in Fig. 4 with general background magnetization $m_z^{\rm b}$.

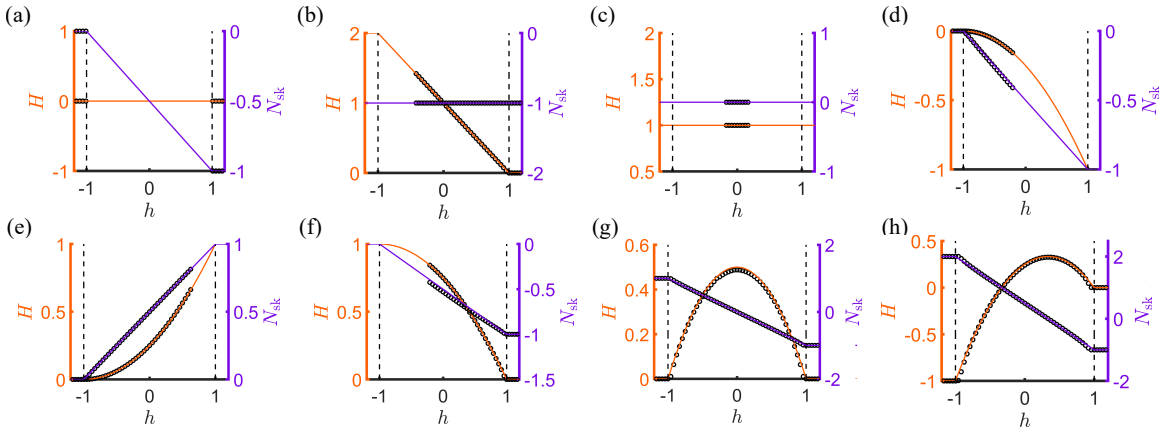

FIG. 5. generalized Hopf index H and Skyrmion number $N_{\rm sk}$ for the magnetic textures depicted in Fig. 4, described by the analytical expressions in Table II (lines). In (b-g) the black circles are the numerically calculated values of $N_{\rm sk}$ and H for the model of Eq. (7), for the range of $|h| < 1.2$, where the texture was numerically stable.

tubes, such that all flux tubes corresponding to the upper and lower subspaces on the S^2 sphere possess flux values of $(1-m_z^{\rm b})/2$ and $(1+m_z^{\rm b})/2$ respectively. The linking numbers, however, remain invariant under variations of $m_z^{\rm b}$, similar to examples from fluid dynamics [49]. In general, $N_{\rm sk}$ [43] and H become a function of $m_z^{\rm b}$ and are continuously tuneable as shown in Table. II.

Changing the magnetization background continuously transforms the magnetic structures considered in Fig. 4. Importantly for $0<|m_z^{\rm b}|<1$, the magnetic textures are in a mixed topology state and can transform smoothly to states with integer Hopf indices, which can be different for tuning the background magnetization up ($m_z^{\rm b}=1$) or down ($m_z^{\rm b}=-1$).

For example, the Skyrmion in a spiral background transforms for $m_z^{\rm b}=1$ into a Skyrmion in a ferromagnetic background with $H=0$. Conversely, for $m_z^{\rm b}=-1$ it becomes an anti-Skyrmion with a self-linking.

The Heliknoton is special in the sense that its topological indices $N_{\rm sk}$ and H do not depend on $m_z^{\rm b}$. Aligning the background continuously along z, the structure transforms to a Hopfion in a ferromagnetic background, i.e. a single closed flux tube as in Fig. 3(d). The (anti-)vortex with self-linking (Fig. 4(d,e) transforms for $m_z^{\rm b}=-1$ to a ferromagnetic state and for $m_z^{\rm b}=1$ to an (anti-)Skyrmion with self-linking. The Twiston transforms for $m_z^{\rm b}=-1$ to a Hopfion with $H=1$ and for $m_z^{\rm b}=1$ to a Skyrmion with $H=0$ as shown in Fig. 3(a). Thus, this texture with $(N_{\rm sk},H)=(-1/2,3/4)$ at $m_z^{\rm b}=0$ can be converted into either a Skyrmion tube or a Hopfion by changing the background (e.g. by an external magnetic field) to a ferromagnetic state. A video showing the transformation between Hopfion and Skyrmion, with the Twiston as the intermediate configuration, is provided as Supplementary Material and described in Sec. III of the Supplementary Material. The screw dislocation with $\nu=2$ transforms for $m_z^{\rm b}=\pm1$ to a Skyrmion with $(N_{\rm sk},H)=(\mp1,0)$. The screw dislocation with $\nu=3$ transforms for $m_z^{\rm b}=1$ to a Skyrmion with $(N_{\rm sk},H)=(-1,0)$, and for $m_z^{\rm b}=-1$ to a pair of braided Skyrmion tubes with $(N_{\rm sk},H)=(2,-1)$.

III. NUMERICAL RESULTS

We employ a specific chiral magnet model to stabilize the examples of topological defects embedded within a non-uniform state, that were considered in the previous section. We emphasize, however, that the methods presented for the calculation of H using Eq. (1) are model-independent.

We consider the energy functional [86]

$$E=\int \mathrm{d}^3r\,[A\,\partial_i\mathbf{m}\cdot\partial_i\mathbf{m}+D\,\mathbf{m}\cdot\boldsymbol{\nabla}\times\mathbf{m}-\mu_0 M_{\rm s}\,\mathbf{H}\cdot\mathbf{m}], \quad (7)$$

where A is the ferromagnetic exchange stiffness, D is the Dzyaloshinskii-Moriya interaction (DMI) strength, $M_{\rm s}$ is the saturation magnetization and $\mathbf{H}$ represents the external magnetic field.

To simplify the analysis, we introduce a dimensionless magnetic field $h=|\mathbf{H}|/H_{\rm c2}$ measured in units of $H_{\rm c2}=D^2/(2A\mu_0 M_{\rm s})$. For an applied magnetic field along the z-direction, the ground state of Eq. (7) is either a ferromagnetic (for $|h|\geq1$) or a (conical) spiral (for $|h|<1$) state. The spiral state is characterized by a wavevector along z with magnitude $q=4\pi A/D$ and

$$\theta=\arccos(h), \quad \phi=qz, \quad (8)$$

in the parametrization of the magnetization given in Eq. (6).

In addition, for $|h|<1$ screw dislocations with Burgers vector ν are also energetically metastable solutions of Eq. (7) [21], with the far field given by

$$\theta=\arccos(h), \quad \phi=\nu\chi+qz. \quad (9)$$

In both cases, conical spiral and screw dislocation, the background magnetization is determined by $m_z^{\rm b}=\cos\theta=h$.

We conduct micromagnetic simulations based on the model in Eq. (7) and relax the textures shown in Fig. 4 for a range of rescaled magnetic field values $-1.2<h<1.2$. Simulations were performed using MuMax3 [87] with the following parameters: exchange stiffness $A=4\times10^{-13}\,\mathrm{J\,m^{-1}}$, bulk DMI constant $D=2.8\times10^{-4}\,\mathrm{J\,m^{-2}}$, and saturation magnetization $M_{\rm s}=1.63\times10^5\,\mathrm{A\,m^{-1}}$. The grid size was set to $(N_x,N_y,N_z)=(360,360,36)$, with a cell size of 0.5 nm, and a cylindrical geometry with a diameter of 180 nm. Periodic boundary conditions were applied along the z-axis, while open boundary conditions were used along the x- and y- axis. Using these parameters, we obtain $L_{\rm D}=4\pi A/D=18\,\mathrm{nm}$ as the period of the spiral along the z-direction, and $\mu_0 H_{\rm c2}=0.6\,\mathrm{T}$ as the critical field for transition to the ferromagnetic state.

Note that depending on the model considered, the textures deform from the ideal textures shown in Fig. 4 upon relaxation, without changing their topological characteristics, see Sec. III of the Supplementary Material.

The numerically calculated values of $N_{\rm sk}$ and H are presented in Fig. 5 (shown as circles) alongside the analytical results (lines) from Table II, showing good agreement (details about the calculation of H are presented in Sec. III of the Supplementary Material). The numerical results are shown for the range of magnetic field values (varied in steps of 0.025 T) where we found the texture to be numerically (meta)stable in this specific model with the numerical implementation chosen. Notably, the analytical expressions in Table II allow us to predict the resulting textures for $|m_z^{\rm b}|=1$, even when these textures are not energetically stable within the model considered.

The model Eq. (7) is invariant under the following simultaneous transformation of magnetization and magnetic field: $\mathbf{m}\to-\mathbf{m}$, $\mathbf{H}\to-\mathbf{H}$. This means that all magnetization configurations exist with two different polarities, which actually have opposite Skyrmion numbers while having the same Hopf index, i.e. $N_{\rm sk}\to-N_{\rm sk}$ and $H\to H$ under this transformation.

IV. CONCLUSION

To conclude, the generalized Hopf index for a continuous field in 3D can be calculated using a discrete formulation (Eq. (1)) providing an alternative to the commonly employed Whitehead integral formula. This discrete approach provides an intuitive interpretation of the generalized Hopf index as a measure of the linkage of flux tubes of the emergent magnetic field. We introduced and implemented this formulation (Eq. (1)) for magnetic textures, demonstrating its utility in quantifying the linkage of flux tubes of the emergent magnetic field of the texture.

Compared to the Whitehead integral formula, this discrete formulation provides a more accessible and intuitive understanding of the generalized Hopf index. Furthermore, while the Whitehead integral can only be computed analytically for a limited set of specific ansatzes [73], the discrete formulation (Eq. (1)) provides precise, model-independent analytical results once the flux tubes and their linking numbers are identified.

We have shown that non-integer values of the generalized Hopf index defined by Eq. (1) naturally occur for magnetic textures with a non-uniform background. We interpret these textures as "mixed topology" states that can smoothly transform into different topological sectors by continuously tuning the background magnetization. While the Skyrmion number and generalized Hopf index vary continuously with the total background magnetization, the linking numbers remain conserved as topological invariants, highlighting their significance as topological characteristics of the texture.

Our results establish a strong physical foundation for the existence of textures with arbitrary non-integer generalized Hopf indices and "mixed topology states", applicable not only in magnetism, but also more generally to solitons in continuous media [14] such as liquid crystals [88], superfluids [7], classical field theories [14], and electromagnetic fields [5], setting the stage for the discovery and investigation of new classes of topological textures across a wide range of materials.

V. ACKNOWLEDGEMENTS

We thank Volodymyr Kravchuk, Markus Garst, Robin Msiska, Finn Feldkamp, Stefan Blügel, Nikolai Kiselev, Jan Masell, Sopheak Sorn, and Philipp Geßler for helpful discussions. This work was supported by the German Research Foundation (DFG) Project No. 505561633 in the TOROID project co-funded by the French National Research Agency (ANR) under Contract No. ANR-22-CE92-0032. We further acknowledge funding from the German Research Foundation (DFG) Project No. 320163632 (Emmy Noether), Project No. 403233384 (SPP2137 Skyrmionics) and Project No. 278162697-SFB 1242 (project B10). M. A. also acknowledges support from the UDE Postdoc Seed Funding.

[1] R. L. Ricca and X. Liu, eds., *Knotted Fields*, Lecture Notes in Mathematics, Vol. 2344 (Springer, Cham, 2024).
[2] D. Kleckner and W. T. M. Irvine, Nat. Phys. **9**, 253 (2013).
[3] A. Neophytou, D. Chakrabarti, and F. Sciortino, Nat. Phys. **18**, 1248 (2022).
[4] T. Ollikainen, A. Blinova, M. Möttönen, and D. S. Hall, Phys. Rev. Lett. **123**, 163003 (2019).
[5] H. Kedia, I. Bialynicki-Birula, D. Peralta-Salas, and W. T. M. Irvine, Phys. Rev. Lett. **111**, 150404 (2013).
[6] D. Han, S. Pal, Y. Liu, and H. Yan, Nat. Nanotechnol. **5**, 712 (2010).
[7] D. Kleckner, L. H. Kauffman, and W. T. M. Irvine, Nat. Phys. **12**, 650 (2016).
[8] U. Tkalec, M. Ravnik, S. Čopar, S. Žumer, and I. Muševič, Science **333**, 62 (2011).
[9] J. Binysh, J. Pollard, and G. P. Alexander, Phys. Rev. Lett. **125**, 047801 (2020).
[10] I. I. Smalyukh, Rep. Prog. Phys. **83**, 106601 (2020).
[11] J.-S. Wu and I. I. Smalyukh, Liq. Cryst. Rev. **10**, 34 (2022).
[12] D. Sugic, R. Droop, E. Otte, D. Ehrmanntraut, F. Nori, J. Ruostekoski, C. Denz, and M. R. Dennis, Nat. Commun. **12**, 6785 (2021).
[13] L. Kong, W. Zhang, P. Li, Z. Wang, C. Meng, H. Jiang, Y. Zhang, S. Liu, S. Yang, J. Sun, S. Zhang, Y. Shen, X. Li, X. Fang, X. Chen, and J. Wang, Nat. Commun. **13**, 2705 (2022).
[14] L. Faddeev and A. J. Niemi, Nature **387**, 58 (1997).
[15] P. Sutcliffe, Phys. Rev. Lett. **118**, 247203 (2017).
[16] F. N. Rybakov, N. S. Kiselev, A. B. Borisov, L. Döring, C. Melcher, and S. Blügel, APL Mater. **10**, 111113 (2022).
[17] N. Kent, N. Reynolds, D. Raftrey, I. T. G. Campbell, S. Virasawmy, S. Dhuey, R. V. Chopdekar, A. Hierro-Rodriguez, A. Sorrentino, E. Pereiro, S. Ferrer, F. Hellman, P. Sutcliffe, and P. Fischer, Nat. Commun. **12**, 1562 (2021).
[18] J.-S. B. Tai and I. I. Smalyukh, Physical Review Letters **121**, 187201 (2018).
[19] P. Sutcliffe, J. Phys. A: Math. Theor. **51**, 375401 (2018).
[20] R. Voinescu, J.-S. B. Tai, and I. I. Smalyukh, Phys. Rev. Lett. **125**, 057201 (2020).
[21] M. Azhar, V. P. Kravchuk, and M. Garst, Phys. Rev. Lett. **128**, 157204 (2022).
[22] F. Zheng, N. S. Kiselev, F. N. Rybakov, L. Yang, W. Shi, S. Blügel, and R. E. Dunin-Borkowski, Nature **623**, 718 (2023).
[23] Y. Duan and X. Liu, J. High Energy Phys. **2004** (02), 028.
[24] J. W. Cirtain, L. Golub, A. R. Winebarger, B. D. Pontieu, K. Kobayashi, R. L. Moore, R. W. Walsh, K. E. Korreck, M. Weber, P. McCauley, A. Title, S. Kuzin, and C. E. DeForest, Nature **493**, 501 (2013).

[25] B. Göbel, I. Mertig, and O. A. Tretiakov, Phys. Rep. **895**, 1 (2021).
[26] C. Back, V. Cros, H. Ebert, K. Everschor-Sitte, A. Fert, M. Garst, T. Ma, S. Mankovsky, T. L. Monchesky, M. Mostovoy, N. Nagaosa, S. S. P. Parkin, C. Pfleiderer, N. Reyren, A. Rosch, Y. Taguchi, Y. Tokura, K. von Bergmann, and J. Zang, J. Phys. D: Appl. Phys. **53**, 363001 (2020).
[27] A. Fert, R. Ramesh, V. Garcia, F. Casanova, and M. Bibes, Rev. Mod. Phys. **96**, 015005 (2024).
[28] Y. Liu and N. Nagaosa, Phys. Rev. Lett. **132**, 126701 (2024).
[29] N. del Ser and V. Lohani, SciPost Phys. **15**, 065 (2023).
[30] J. Tang, Y. Wu, W. Wang, L. Kong, B. Lv, W. Wei, J. Zang, M. Tian, and H. Du, Nat. Nanotechnol. **16**, 1086 (2021).
[31] E. Barts and M. Mostovoy, npj Quantum Mater. **6**, 104 (2021).
[32] Y. Zhang, J. Tang, Y. Wu, M. Shi, X. Xu, S. Wang, M. Tian, and H. Du, Nat. Commun. **15**, 3391 (2024).
[33] W. Lin, N. Mata-Cervera, Y. Ota, Y. Shen, and S. Iwamoto, Space-time optical hopfion crystals (2025).
[34] X. S. Wang, A. Qaiumzadeh, and A. Brataas, Phys. Rev. Lett. **123**, 147203 (2019).
[35] B. Göbel, C. A. Akosa, G. Tatara, and I. Mertig, Phys. Rev. Res. **2**, 013315 (2020).
[36] Y. Liu, W. Hou, X. Han, and J. Zang, Phys. Rev. Lett. **124**, 127204 (2020).
[37] D. Raftrey and P. Fischer, Phys. Rev. Lett. **127**, 257201 (2021).
[38] J. C. Bellizotti Souza, C. J. O. Reichhardt, C. Reichhardt, A. Saxena, N. P. Vizarim, and P. A. Venegas, Scientific Reports **15**, 16802 (2025).
[39] X. Yu, Y. Liu, K. V. Iakoubovskii, K. Nakajima, N. Kanazawa, N. Nagaosa, and Y. Tokura, Adv. Mater. **35**, 2210646 (2023).
[40] W. S. Parker, J. A. Reddinger, and B. J. McMorran, Phys. Rev. B **110**, 224420 (2024).
[41] S.-Z. Lin, A. Saxena, and C. D. Batista, Phys. Rev. B **91**, 224407 (2015).
[42] X. Z. Yu, W. Koshibae, Y. Tokunaga, K. Shibata, Y. Taguchi, N. Nagaosa, and Y. Tokura, Nature **564**, 95 (2018).
[43] N. del Ser, I. El Achchi, and A. Rosch, Phys. Rev. B **110**, 094442 (2024).
[44] F. N. Rybakov, O. Eriksson, and N. S. Kiselev, Phys. Rev. B **111**, 134417 (2025).
[45] A. O. Leonov, T. L. Monchesky, J. C. Loudon, and A. N. Bogdanov, J. Phys. Condens. Matter **28**, 35LT01 (2016).
[46] F. N. Rybakov, A. B. Borisov, S. Blügel, and N. S. Kiselev, Phys. Rev. Lett. **115**, 117201 (2015).
[47] V. M. Kuchkin, N. S. Kiselev, F. N. Rybakov, I. S. Lobanov, S. Blügel, and V. M. Uzdin, Front. Phys. **11** (2023).
[48] J. Milnor, Ann. Math. **59**, 177 (1954).
[49] H. K. Moffatt, Proc. Natl. Acad. Sci. **111**, 3663 (2013).
[50] T. Machon, Liq. Crys. Today **28**, 58 (2019).
[51] S. Čopar and S. Žumer, Phys. Rev. Lett. **106**, 177801 (2011).
[52] M. W. Scheeler, W. M. van Rees, H. Kedia, D. Kleckner, and W. T. M. Irvine, Science **357**, 487 (2017).
[53] D. Auckly and L. Kapitanski, Commun. Math. Phys. **256**, 611 (2005).
[54] J. Jäykkä and J. Hietarinta, Phys. Rev. D **79**, 125027 (2009).
[55] M. Kobayashi and M. Nitta, Nucl. Phys. B **876**, 605 (2013).
[56] R. Balakrishnan, R. Dandoloff, and A. Saxena, Phys. Lett. A **480**, 128975 (2023).
[57] R. Knapman, T. Tausendpfund, S. A. Díaz, and K. Everschor-Sitte, Commun. Phys. **7**, 151 (2024).
[58] R. Balakrishnan, R. Dandoloff, and A. Saxena, Phys. Lett. A **493**, 129261 (2024).
[59] P. J. Ackerman and I. I. Smalyukh, Phys. Rev. X **7**, 011006 (2017).
[60] A. Samoilenka and Y. Shnir, J. High Energy Phys. **2017** (9), 29.
[61] M. A. Berger and G. B. Field, J. Fluid Mech. **147**, 133–148 (1984).
[62] C. Prior and A. R. Yeates, Astrophys. J. **787**, 100 (2014).
[63] J. J. Moreau, C. R. Acad. Sci. **252**, 2810 (1961).
[64] H. K. Moffatt, J. Fluid. Mech. **35**, 117–129 (1969).
[65] H. Moffatt, *Magnetic Field Generation in Electrically Conducting Fluids* (Cambridge University Press, 1978).
[66] H. K. Moffatt, J. Fluid. Mech. **106**, 27–47 (1981).
[67] Please note that every solenoidal vector field can be decomposed into flux tubes. This decomposition is not necessarily unique, but all decompositions lead to the same result in Eq. (1). For a definition of flux tubes we refer to Ref. [62].
[68] H. K. Moffatt and R. L. Ricca, Proc. Roy. Soc. Lond. A **439**, 411 (1992).
[69] R. L. Ricca and H. K. Moffatt, The helicity of a knotted vortex filament, in *Topological Aspects of the Dynamics of Fluids and Plasmas*, edited by H. K. Moffatt, G. M. Zaslavsky, P. Comte, and M. Tabor (Springer Netherlands, Dordrecht, 1992) pp. 225–236.
[70] Equation (2) contains integrals over closed curves. For field lines that run vertically along the z-direction, the periodic boundary conditions imply that the field lines close trivially at infinity. An alternative is to define "winding numbers" of open field lines as in Ref. [62].
[71] Note that, in general, linking numbers can be written as the sum of twist and writhe components [49–52].
[72] J. Whitehead, PNAS **33**, 117 (1947).
[73] H. J. de Vega, Phys. Rev. D **18**, 2945 (1978).
[74] K. Y. Guslienko, Chaos, Solitons & Fractals **174**, 113840 (2023).
[75] R. Knapman, M. Azhar, A. Pignedoli, L. Gallard, R. Hertel, J. Leliaert, and K. Everschor-Sitte, Phys. Rev. B **111**, 134408 (2025).
[76] G. E. Volovik, J. Phys. C: Solid State Phys. **20**, L83 (1987).
[77] K. Everschor-Sitte and M. Sitte, J. Appl. Phys. **115**, 172602 (2014).
[78] The total Skyrmion number N_{sk} calculated by integrating $\mathbf{F}$ over the entire (x, y)-plane generally differs from the individual $N_{\mathrm{sk},i}$. For instance, toroidal flux tubes are confined entirely within the sample and do not contribute to the net vertical flux.
[79] S. M. Barnett, F. C. Speirits, and J. B. Götte, Europhys. Lett. **143**, 35002 (2023).
[80] Please see App. IV for a comparison of the calculation of the Hopf index using physical boundary conditions and a nested box approach [22].
[81] For the examples discussed in these sections—as well as for many textures reported in the literature—the flux

tube representation involving up to three tubes provides an intuitive and effective geometric framework. Nonetheless, more intricate textures may require a larger number of flux tubes to accurately describe their structure.

[82] R. Zarzuela, V. K. Bharadwaj, K.-W. Kim, J. Sinova, and K. Everschor-Sitte, Phys. Rev. B **101**, 054405 (2020).

[83] B. Göbel, A. Mook, J. Henk, I. Mertig, and O. A. Tretiakov, Phys. Rev. B **99**, 060407 (2019).

[84] (referred to as sd_1^+ and sd_{-1}^+ in Ref. [21]).

[85] (referred to as $\mathrm{sd}_1^{\mathrm{Sk}-}$ in Ref. [21]).

[86] I. E. Dzyaloshinskii, J. Exptl. Theoret. Phys. (U.S.S.R.) **46**, 1420 (1964).

[87] A. Vansteenkiste, J. Leliaert, M. Dvornik, M. Helsen, F. Garcia-Sanchez, and B. Van Waeyenberge, AIP Adv. **4**, 107133 (2014).

[88] J.-S. B. Tai, P. J. Ackerman, and I. I. Smalyukh, Proc. Natl. Acad. Sci. **115**, 921 (2018).

[89] D. MacTaggart and A. Valli, Journal of Plasma Physics **85**, 775850501 (2019).

Supplementary Materials

I. LINKING NUMBERS AND THE HOPF INDEX

A. Linking numbers

The convention for linking numbers followed in this paper is given by the formula in Eq. (2), and sketched in Fig. 2 of the main text. Reversing the direction on any contour reverses the sign of the linking number, as shown in Fig. S1.

B. Whitehead formula in terms of linking numbers

We demonstrate in a two-step approach that the Whitehead formula for the Hopf index is equivalent to the expression in Eq. (1). In the first step following Ref. [64], we only consider flux tubes without self-linking, and in the second step, we generalize this result to tubes with self-linking following Ref. [68].

Step 1: To begin, we consider cases in which the vector field $\mathbf{F}$ can be decomposed in the volume V into flux tubes without self-linking, i.e. where Eq. (1) reduces to the second term $\sum_i \sum_{j\neq i} L_{ij}\Phi_i\Phi_j$. Here, Φ_i is the flux flowing within tube i as defined in the main text.

We first show that the Whitehead integral formula, $H = \int_V \mathbf{F}\cdot\mathbf{A}\,\mathrm{d}V$ is equivalent to $\sum_i \varphi_i\Phi_i$, where φ_i is

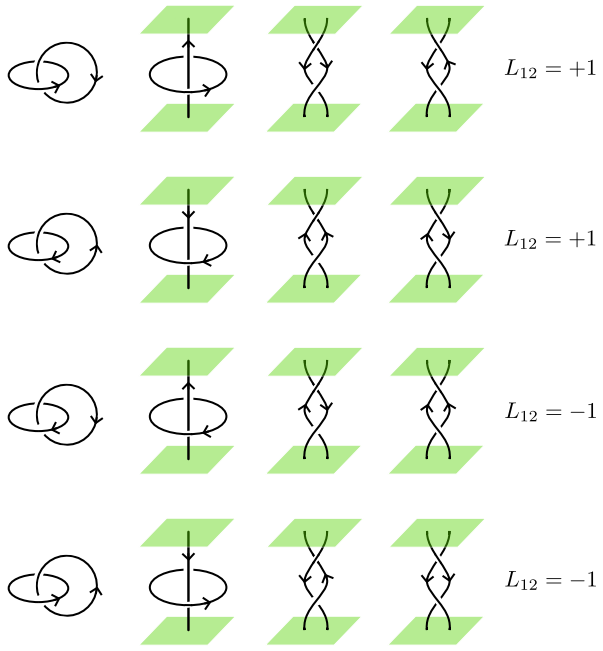

FIG. S1. The values of the linking numbers L_{12} for two oriented curves, calculated using the formula given in Eq. (2). $L_{12} = 1$ for the first two rows and $L_{12} = -1$ for the last two rows.

the flux of $\mathbf{F}$ piercing the disc surface $\mathbf{S}_i$ formed by a contour C_i along a streamline of tube i (see Fig. S2). To show this, the volume integral in the Whitehead formula can be decomposed into the individual contributions of the flux tubes

$$H = \int_V \mathbf{F}\cdot\mathbf{A}\,\mathrm{d}V \tag{10a}$$

$$= \sum_i \int_{V_i} \mathbf{F}\cdot\mathbf{A}\,\mathrm{d}V \tag{10b}$$

$$= \sum_i \oint_{C_i} \mathrm{d}r \int_{\mathbf{a}_i} \mathrm{d}a\,(\mathbf{F}\cdot\mathbf{A}), \tag{10c}$$

where the last equal sign makes use of the fact that a volume integral of a flux tube can generally be formed along and perpendicular to any chosen contour $C_i \in V_i$ for thin tubes where $\mathbf{a}_i \ll \mathbf{S}_i$. Here, $\mathbf{a}_i$ is the cross-sectional area of the tube. We introduce the unit vector $\hat{\mathbf{f}} = \mathbf{F}/|\mathbf{F}|$, to rewrite H in the factorized form:

$$H = \sum_i \oint_{C_i} \mathrm{d}r \int_{\mathbf{a}_i} \mathrm{d}a\,(\mathbf{F}\cdot\hat{\mathbf{f}})(\mathbf{A}\cdot\hat{\mathbf{f}}) \tag{11a}$$

$$= \sum_i \oint_{C_i} \int_{\mathbf{a}_i} (\mathbf{F}\cdot\mathrm{d}\mathbf{a})(\mathbf{A}\cdot\mathrm{d}\mathbf{r}), \tag{11b}$$

where $\mathrm{d}\mathbf{r} = \hat{\mathbf{f}}\,\mathrm{d}r$ and $\mathrm{d}\mathbf{a} = \hat{\mathbf{f}}da$. For such thin flux tubes with bounding surfaces of genus 1, the oriented area element $\mathrm{d}\mathbf{a}$ and the line element $\mathrm{d}\mathbf{r}$, are parallel to $\mathbf{F}$ inside the tube. Also, the flux $\mathbf{F}\cdot\mathrm{d}\mathbf{a}$ is independent of the path variable r, as required by flux conservation and the condition $\nabla\cdot\mathbf{F} = 0$. Therefore we can first integrate over C_i, or equivalently, decouple the integrals over C_i and $\mathbf{a}_i$ as,

$$H = \sum_i \left(\int_{\mathbf{a}_i} \mathbf{F}\cdot\mathrm{d}\mathbf{a}\right)\left(\oint_{C_i} \mathbf{A}\cdot\mathrm{d}\mathbf{r}\right). \tag{12}$$

The first factor is the flux Φ_i as defined in the main text. Using Stokes theorem, the second factor can be expressed as the flux φ_i piercing the loop C_i, see Fig. S2,

$$\oint_{C_i} \mathbf{A}\cdot\mathrm{d}\mathbf{r} = \int_{\mathbf{S}_i} \mathbf{F}\cdot\mathrm{d}\mathbf{a} = \varphi_i. \tag{13}$$

Now, we introduce the linking number L_{ij} which equals the signed number of times the tube j intersects the area $\mathbf{S}_i$. Therefore, φ_i can be expressed in terms of the linking numbers L_{ij} between C_i and C_j in the following way:

$$\varphi_i = \sum_{j\neq i} L_{ij}\Phi_j. \tag{14}$$

This then completes the proof

$$H = \int_V \mathbf{F}\cdot\mathbf{A}\,\mathrm{d}V = \sum_i \varphi_i\Phi_i = \sum_i \sum_{j\neq i} L_{ij}\Phi_i\Phi_j, \tag{15}$$

for cases in which the vector field $\mathbf{F}$ can be decomposed in the volume V into flux tubes without self-linking.

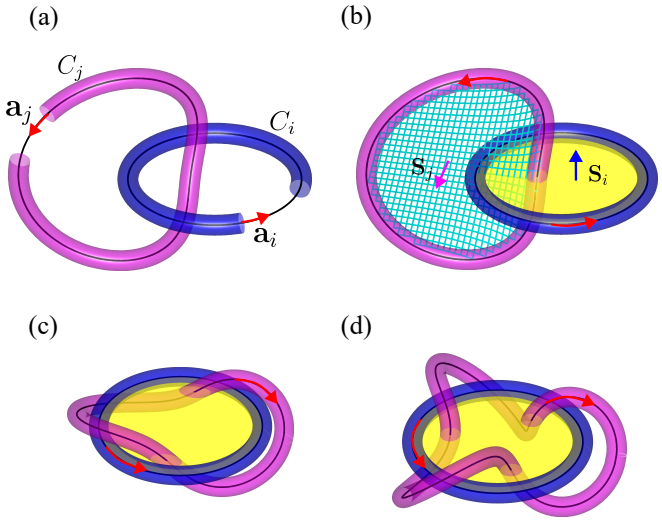

FIG. S2. Two flux tubes of the vector field $\mathbf{F}$, labeled i and j, with their respective bounding surfaces colored magenta and blue. The red arrows indicate the direction of $\mathbf{F}$ within the tubes. (a) A cut through the bounding surfaces of i and j reveals the contours C_i and C_j which are streamlines of $\mathbf{F}$ passing through the tubes, along with their corresponding cross-sectional areas $\mathbf{a}_i$ and $\mathbf{a}_j$. (b) The yellow-shaded area $\mathbf{S}_i$, enclosed by C_i, and the cyan-meshed area $\mathbf{S}_j$, enclosed by C_j, are oriented according to the right-hand rule, as indicated by the blue and magenta arrows. The inter-linking number L_{ij} is 1 for panels (a) and (b), 2 for (c), and 3 for (d). The total flux φ_i through $\mathbf{S}_i$ is determined by the number of times the flux line j pierces $\mathbf{S}_i$, multiplied by its flux Φ_j, i.e. $\varphi_i = L_{ij}\Phi_j$.

While we considered thin flux tubes, the result obtained is universal for any system of non-overlapping flux tubes (with bounding surfaces of genus 1) without self-linking, regardless of their thickness. This universality arises because H remains invariant under flux-conserving continuous deformations of the field lines of $\mathbf{F}$, implying that such systems, being related through these deformations, are topologically equivalent. Note that substituting $\Phi_i = \sum_{j\neq i} L_{ij}\varphi_j$ into $H = \sum_i \varphi_i\Phi_i$ yields the equivalent expression, $H = \sum_i \sum_{j\neq i} L_{ij}\varphi_i\varphi_j$.

Step 2: Let us now consider the general case that permits self-linking. We demonstrate that it can be mapped to the case considered in step 1, where self-linking is absent.

Since self-linking contributions are summed independently for each flux tube, it suffices to consider a single flux tube with uniform self-linking number L, meaning that any pair of streamlines of $\mathbf{F}$ within the tube have the same inter-linking number L. The tube is divided into N thin filaments, each carrying a flux Φ/N (as illustrated in Sec. II for a Skyrmion and a Hopfion). In the limit $N \to \infty$ it is justified to assume that each of the filaments has zero self-linking but a constant inter-linking number L. Using the relation $H = \sum_i \sum_{j\neq i} L_{ij}\Phi_i\Phi_j$, from step 1 for the $N!/(N-2)!$ number of pairs of filaments, one obtains:

$$H = L\frac{N!}{(N-2)!}\left(\frac{\Phi}{N}\right)^2. \tag{16}$$

In the limit $N \to \infty$, this expression simplifies to

$$H = L\Phi^2, \tag{17}$$

which corresponds to the first term in Eq. (1) for a single flux tube with flux Φ and self-linking L.

It is important to note that subdividing a flux tube into smaller tubes conserves the total value of H, it just shifts weight from the first term to the second one.

II. DIVISION OF VECTOR FIELD INTO FLUX TUBES

Per definition, the boundaries of a flux tube is a surface S with $\mathbf{F}\cdot\hat{n}|_S = 0$, i.e. the field lines of $\mathbf{F}$ cannot enter or leave this surface. The assignment of $\mathbf{F}$ to flux tubes for an arbitrary spin texture is, however, not unique. We illustrate this with specific examples of a Skyrmion with self-linking (Sec. II A), a Hopfion (Sec. II B) in a ferromagnetic background and a Heliknoton (Sec. II C).

A. Flux division for one Skyrmion

For a Skyrmion with self-linking, shown in Fig. S3(a), the Hopf index is given by $H = L_{11}\Phi_1 = -1$, if we assign all flux to a single flux tube. As an alternative, we can choose a division into two concentric nested tubes as shown in Fig. S3(b) or two braided tubes as shown in Fig. S3(c). The Hopf index is then given by $H = L_{11}\Phi_1 + L_{22}\Phi_2 + 2L_{12}\Phi_1\Phi_2 = -1/4 - 1/4 - 1/2 = -1$.

B. Hopf index for N number of sub-tubes constituting one Hopfion

A Hopfion can, for example, be considered as a single flux tube with total flux Φ and linking number L, or it can be decomposed into N equivalent linked flux tubes each with flux Φ/N and self- and inter-linking numbers all being L, see Fig. S4. In the first case, the Hopf index is $H = L\Phi^2$, and in the second case

$$H = NL\left(\frac{\Phi}{N}\right)^2 + 2\binom{N}{2}L\left(\frac{\Phi}{N}\right)^2 = L\Phi^2, \tag{18}$$

where the first term is the contribution to the Hopf index due to the N tubes self-linking each with linking number L, and the second term is the interlinking contribution. The binomial factor $\binom{N}{2}$ enters due to the number of possibilities to choose 2 out of N flux tubes.

Note that in the limit $N \to \infty$ the self-linking contribution scales as $\sim 1/N$ whereas the inter-linking contribution has a part that scales independently of N in

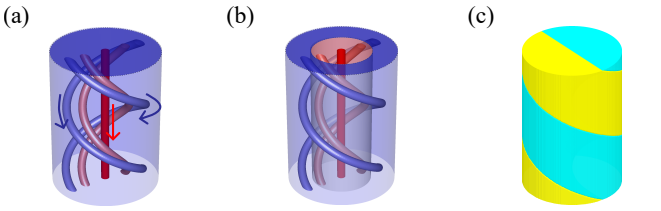

FIG. S3. Skyrmion tube in a ferromagnetic background ($m_z^{\mathrm{b}} = 1$) with self-linking, depicted for three different flux tube decompositions: (a) single flux tube, (b) two concentric flux tubes shown as blue and red surfaces, each with flux $\Phi = 1/2$, and (c) two braided flux tubes shown as yellow and cyan surfaces, each with flux $\Phi = 1/2$. The blue and red thin tubes depict a selection of the field lines of $\mathbf{F}$, with arrows showing the direction of $\mathbf{F}$. Independent of the flux tube decomposition, all three configurations yield a Hopf index of $H = -1$.

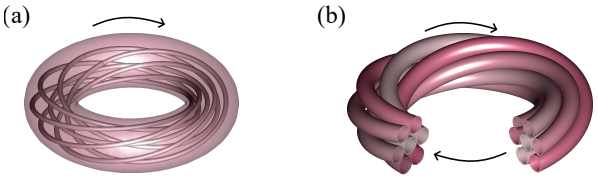

FIG. S4. Sketches of flux decompositions of the vector field $\mathbf{F}$ for a Hopfion (a) as a single flux tube, (b) into several linked flux tubes. The arrow indicates the direction of $\mathbf{F}$.

agreement with our assumption made in Sec. I B, that any texture can be decomposed into a large number of flux tubes that only have interlinking contributions.

C. Topological decomposition for a Heliknoton

Magnetic textures can be decomposed into their constituent topological textures. As an example, consider the Heliknoton (Fig. 4(c)) that can be decomposed into the sum of a screw dislocation with $\nu = -1$ (Fig. 4(e)) and a screw dislocation with $\nu = 1$ (Fig. 4(f)). The Hopf index sums to 1 at any value of m_z^{b}, demonstrating the additivity of the H when two simply connected volumes are merged while deforming $\mathbf{F}$ near the surface, to preserve the continuity of $\mathbf{F}$. An illustration of this concept is shown in Fig. S5 where the $\mathbf{F}$ constituting the Heliknoton is shown to be split into two components.

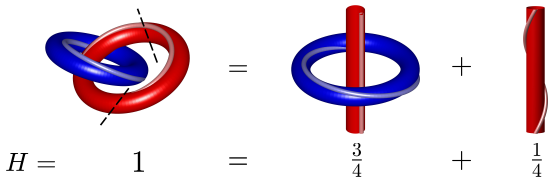

FIG. S5. The emergent magnetic field $\mathbf{F}$ comprising the Heliknoton can be cut along the dashed lines to be decomposed into the sum of two constituents: the Twiston and an antivortex meron with a self-linking. There are periodic boundary conditions along the z direction in all cases. The blue and red tubes represent flux tubes of $\mathbf{F}$ with $m_z > 0$ and $m_z < 0$ in their interior respectively. The light blue(red) line represents one field line of $\mathbf{F}$.

III. ADDITIONAL NUMERICS

A. Numerically relaxed magnetic textures

We show details of numerically relaxed textures, the Skyrmion in a spiral background (Fig. S8) and the Twiston (Fig. S9). The vector field $\mathbf{F}$ is plotted for cross-sections in the yz-, xz- and xy-planes in panels (i) to (l) of Figs. S8 and S9. Along the x and y directions, $\mathbf{F} \to \mathbf{0}$ as $x \to \infty$ or $y \to \infty$ for all textures considered.

B. Choice of gauge potential

The Hopf index, calculated using the Whitehead equation $H = \int_V \mathrm{d}^3 r\, \mathbf{F} \cdot \mathbf{A}$ for a finite integration volume V, is gauge invariant when $\mathbf{F} \cdot \hat{\mathbf{n}}$ vanishes at the surfaces of V (where $\hat{\mathbf{n}}$ is the surface normal) [75]. However, if $\mathbf{F}$ does not satisfy these boundary conditions—for example, when the field lines of $\mathbf{F}$ run along the z-axis and intersect the top and bottom surfaces of V with periodic boundary conditions along z, then the base space becomes a $S^2 \times S^1$ and H is a topological invariant only when it is measured relative to a reference state [61, 62].

As a natural reference state, we consider a translationally invariant Skyrmion tube which must have the trivial Hopf index of 0 (see Fig. 3(a)) using the chosen gauge. In addition, when $\mathbf{F}$ is periodic, $\mathbf{A}$ must satisfy the same periodic boundary conditions.

In the $S^2 \times S^1$ setting, the Whitehead integral generally acquires additional terms to preserve its gauge invariance [89]. The purpose of gauge fixing in an $S^2 \times S^1$ topology is to to ensure that these extra contributions vanish. This requirement imposes restrictions on the admissible forms of the gauge potential $\mathbf{A}$ [58]. Admissable gauge choices include the winding gauge [62], which satisfies $\partial_x A_x + \partial_y A_y = 0$, and gauges with $A_x = 0$ or $A_y = 0$, such as the one used in Eq. (19) below.

A gauge that yields a trivial Hopf index for a translationally invariant Skyrmion tube along the z-direction

is

$$\begin{aligned} A_x(x,y,z) &= -\int_{-L_{y/2}}^{y} \mathrm{d}y' F_z(x,y',z), \\ A_y(x,y,z) &= 0, \\ A_z(x,y,z) &= \int_{-L_{y/2}}^{y} \mathrm{d}y' F_x(x,y',z). \end{aligned} \tag{19}$$

This gauge is used for our numerical calculations of the generalized Hopf index H, consistent with Ref. [75]. $L_x(L_y)$ are dimensions of the integration volume along the $x(y)$-direction. L_x and L_y must be large enough so that $\mathbf{F} \approx \mathbf{0}$ at $x = \pm L_x/2$ and $y = \pm L_y/2$, yet sufficiently smaller than the full simulated geometry, to exclude contributions from chiral surface twists at the lateral edges of the geometry. For the results presented in Fig. 5, sufficiently accurate results for H are obtained by using an integration volume with $L_x = L_y = 5L_D$ where L_D is the size of the integration volume along the z direction, and the full simulation geometry is a disc with diameter $10L_D$ and height L_D, ensuring that the chiral surface effects lie outside the integration region. For the heliknoton (Fig. 5(c)), the size of the integration volume as well as the simulation geometry was chosen to be $L_x = L_y = L_z = 5L_D$. Furthermore, $\mathbf{F}$ is calculated using the average solid angle between neighboring lattice sites as in Ref. [75].

C. Accounting for arbitrary background values $m_z^{\mathrm{b}} = h$

A video illustrating the continuous transformation from Hopfion to Twiston to Skyrmion is provided in the Supplementary Material. Stills from this video are shown in Fig. S6.

While the Twiston-to-Skyrmion transition can be stabilized within the chiral magnet model described in Ref. [21], the Twiston-to-Hopfion transition is not energetically stable throughout the full range of $h < 0$, as indicated by the absence of black circles in Fig. 5(f). Therefore, we adopt a different approach that reproduces the desired transitions starting from a reference configuration at $m_z^{\mathrm{b}} = h = 0$.

To generate configurations corresponding to arbitrary background values $m_z^{\mathrm{b}} = h \neq 0$, we begin with the Twiston texture, which is stable at zero applied magnetic field. We choose the texture with core polarity $p = -1$, as illustrated in Fig. 4(f) and Fig. S9(c). We then remap the polar angle $\theta = \arccos(m_z)$, while preserving the azimuthal angle $\phi = \mathrm{atan2}(m_y, m_x)$. This transformation adjusts the latitude of the far-field magnetization to match the value defined by h on the unit sphere. Specifically, we use:

$$\theta' = \begin{cases} m_1 \cdot \theta + c_1, & \text{for } -1 \leq h < 0, \\ m_2 \cdot \theta + c_2, & \text{for } 0 \leq h \leq 1. \end{cases} \tag{20}$$

where

$$\begin{aligned} m_1 &= \frac{\arccos(h)}{\pi/2}, & c_1 &= 0, \\ m_2 &= \frac{\pi - \arccos(h)}{\pi/2}, & c_2 &= 2\left(-\frac{\pi}{2} + \arccos(h)\right). \end{aligned}$$

The remapped polar angle is clipped such that $\theta' \in [0, \pi]$. This ensures the transformed magnetization field $\mathbf{m} = (\cos\phi \sin\theta', \sin\phi \sin\theta', \cos\theta')$ is properly normalized and gives the correct far-field, as $\lim_{|\mathbf{r}_\perp| \to \infty} m_z = m_z^{\mathrm{b}}$ for $\mathbf{r}_\perp = (x, y)$. This procedure enables us to construct spin textures with a tunable background magnetization $m_z^{\mathrm{b}} = h$.

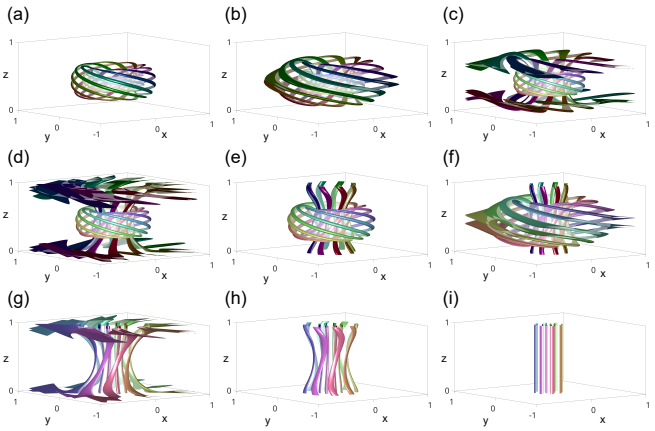

FIG. S6. Selected snapshots from the continuous transition from a Hopfion to a Skyrmion, achieved by varying the background magnetization m_z^{b} from -1 to 1. Panels (a) to (i) correspond to configurations at $m_z^{\mathrm{b}} = -1$, -0.75, -0.33, 0, 0.29, 0.58, 0.75, and 1, respectively. In each snapshot, isolines of the magnetization are shown at $m_z = \pm 0.5$ for eight different azimuthal angles ϕ. The associated values of N_{sk} and H are presented in Fig. 5(f) of the main text.

IV. COMPARISON OF THE HOPF INDEX CALCULATION OF PHYSICAL BOUNDARIES WITH THE NESTED BOX FRAMEWORK FOR TEXTURES IN A $S^2 \times S^1$ BASE SPACE

A differently defined Hopf index, denoted as H^{nested} in the following, was introduced in Ref. [22] for textures with a $S^2 \times S^1$ base space. This method, known as the "nested box approach," involves continuously embedding a periodic magnetic texture along the z-direction into a larger box, with fixed boundary conditions $\mathbf{m}(\mathbf{r}) \to \mathbf{m}_0$ imposed on the lateral surfaces; see Fig. S7. This construction yields an integer-valued skyrmion number $N_{\mathrm{sk}}^{\mathrm{nested}} \in \mathbb{Z}$ and an integer-valued $H^{\mathrm{nested}} \in \mathbb{Z}$, in agreement with Eqs. (4) and (5). Unfortunately, the nested box method attributes a substantial portion of the computed values $N_{\mathrm{sk}}^{\mathrm{nested}}$ and H^{nested} to $N_{\mathrm{sk}}^{\mathrm{outer}}$ and H^{outer}, originating from the region outside the physical sample.

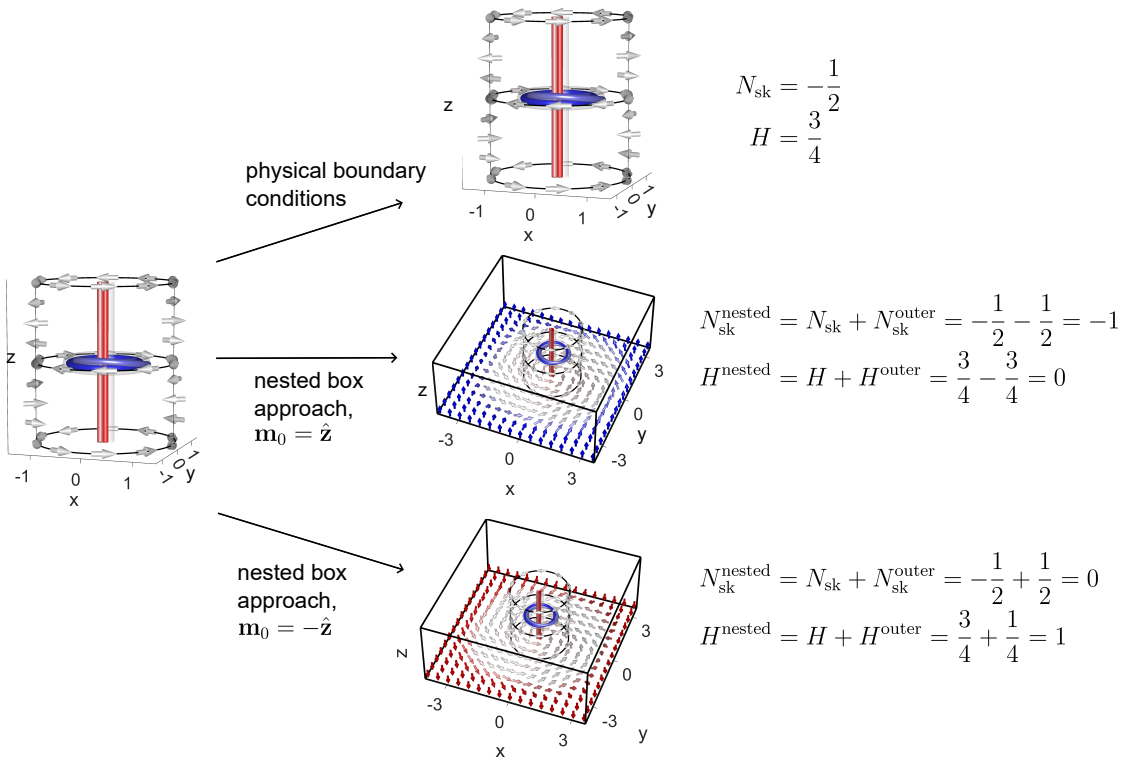

FIG. S7. Comparison of a Hopf index calculation using physical boundary conditions yielding H and using the nested box approach giving $H^{\rm nested}$—where the sample is embedded in a larger computational volume with fixed boundary conditions $\mathbf{m} = \hat{\mathbf{z}}$ or $\mathbf{m} = -\hat{\mathbf{z}}$ on the lateral surfaces—exemplified on a Twiston, which is also shown in Fig. 4(f). Notably, the nested box approach yields integer values as outer embedding also contributes to $H^{\rm nested} = H + H^{\rm outer}$. Importantly, the embedding cannot be uniquely defined, as depicted in the figure, which has implications for the value of $H^{\rm outer}$ and thus $H^{\rm nested}$. Arrows indicate the direction of the magnetization $\mathbf{m}$, using the same color scheme as in Fig. 1.

Furthermore, the result of $N_{\rm sk}^{\rm nested}$ and $H^{\rm nested}$ are not unique and depend on the direction chosen for the ferromagnetic embedding, see Fig. S7 and Table S1 for more examples.

In contrast, our approach does not employ a nested box. Instead, we restrict the integration volume to the physical sample, allowing $\mathbf{m}(\mathbf{r})$ to remain non-uniform at the side boundaries (defined naturally where $\mathbf{F} \approx \mathbf{0}$). This is essential for capturing the continuous topological evolution of arbitrary $S^2 \times S^1$ base-space textures, which generally yield non-integer values of the Skyrmion number and generalized Hopf index, i.e. $N_{\rm sk} \in \mathbb{R}$ and $H \in \mathbb{R}$.

Another discrepancy appears when we consider the operation $\mathbf{m} \to -\mathbf{m}$ under which the Whitehead integral as well as Eq. (1) is invariant, i.e. $H \to H$. This symmetry reflects the topological nature of H as a measure of field line linking, insensitive to the overall orientation of the magnetization—a property also shared by the linking numbers. However, in the nested-box approach, this flip-invariance no longer holds when the background magnetization is noncollinear: if one first inverts $\mathbf{m} \to -\mathbf{m}$ in the physical sample and then computes the Hopf index using the same reference orientation $\mathbf{m}_0$ for the nested box, the resulting $H^{\rm nested}$ differs.

	$h = -1$ **Hopfion**	$h = 0$ **Twiston**	$h = 1$ **Skyrmion tube**
$(N_{\rm sk}, H)$ using physical boundary conditions	(0,1)	$\left(-\frac{1}{2}, \frac{3}{4}\right)$	(−1,0)
$(N_{sk}^{\rm nested}, H^{\rm nested})$ in nested box approach with $\boldsymbol{m}_0 = \hat{z}$	(−1,1)	(−1,0)	(−1,0)
$(N_{sk}^{\rm nested}, H^{\rm nested})$ in nested box approach with $\boldsymbol{m}_0 = -\hat{z}$	(0,1)	(0,1)	(0,0)

TABLE S1. Skyrmion number and Hopf index calculated using i) physical boundary conditions, ii) nested box approach from Ref. [32] with $\mathbf{m}_0 = \hat{\mathbf{z}}$ and iii) nested box approach with $\mathbf{m}_0 = -\hat{\mathbf{z}}$, for the Hopfion in a ferromagnetic background with $m_z^{\rm b} = -1$, a Twiston (see Fig. 4(f)), and a Skyrmion tube in a ferromagnetic background with $m_z^{\rm b} = +1$. Interestingly, in the nested box approach, the Twiston is assigned the same topological indices as a"Hopfion" or "Skyrmion tube" solely depending on the imposed boundary condition $\mathbf{m}_0$.

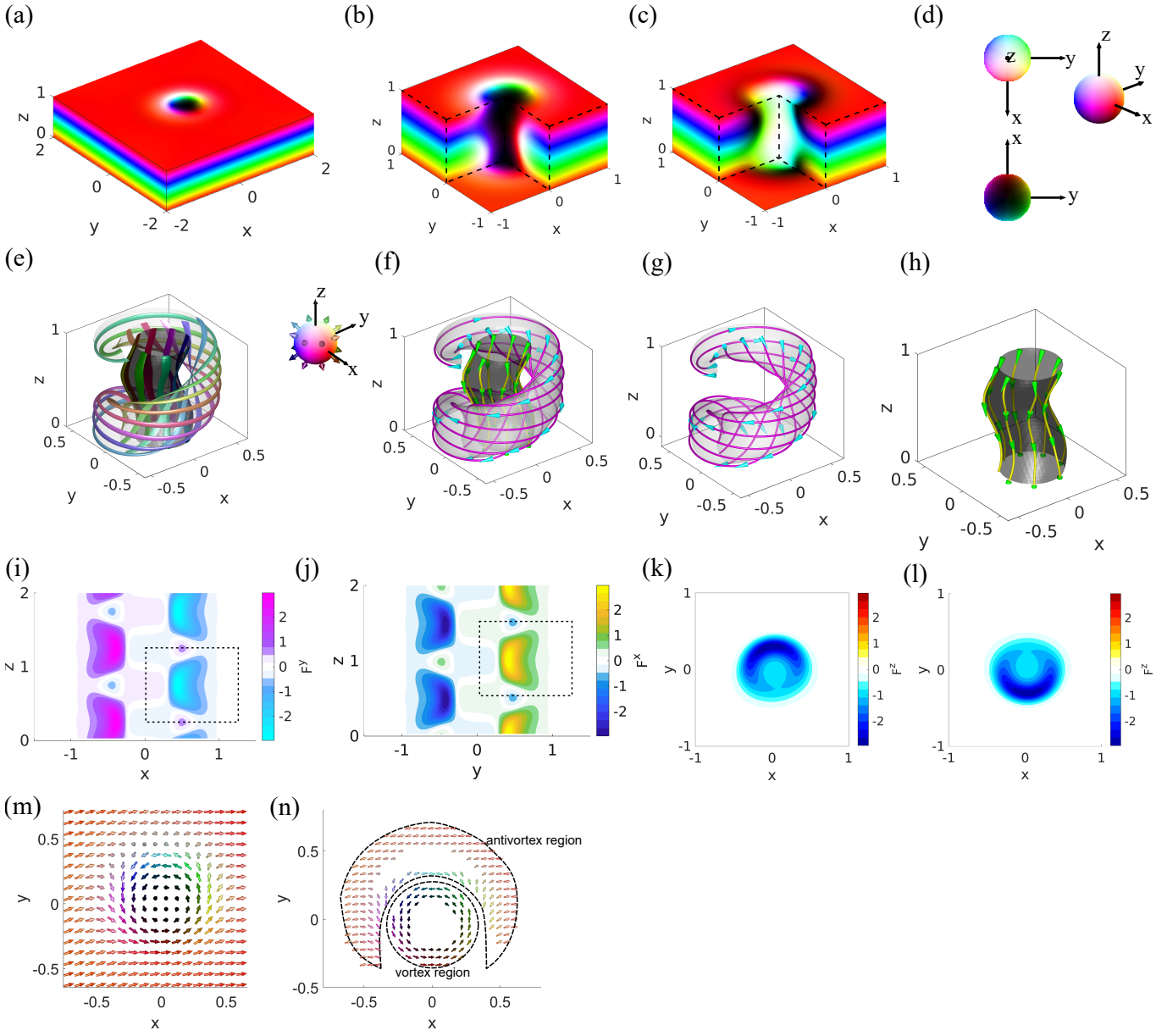

FIG. S8. Numerically relaxed magnetization configuration of the Skyrmion string aligned along the z-axis in a helical spiral background with spiral wavevector also along the z direction. (a) displays a box of height L_{D}, centred on the Skyrmion string at $(x, y) = (0, 0)$. The HSL colourmap shown in (d) is used to represent the magnetization direction $\mathbf{m}$ in panels (a) to (c). In (a) and (b) the xy-plane features a vortex (black) and an antivortex tube (white), with cores polarized along $-z$ and $+z$ respectively. (b) and (c) show cuts through the centre of the box, for Skyrmions with $(N_{\mathrm{sk}}, H) = (-1, -1)$ and $(N_{\mathrm{sk}}, H) = (1, -1)$, respectively, that are related by the transformation $\mathbf{m} \to -\mathbf{m}$, $z \to z + 0.5$. (e) shows selected preimages of magnetization for $m_z = \pm 0.5$, overlaid on the isosurfaces of $m_z = \pm 0.5$. (f) depicts the field lines of the emergent magnetic field $\mathbf{F}$, overlaid on the isosurfaces of $m_z = \pm 0.5$. The arrows depict the direction of $\mathbf{F}$. (g) and (h) separately display the data from (f) for $m_z = +0.5$ and $m_z = -0.5$, respectively. (i) and (j) present plots of F_x and F_y, respectively, with each half-plane (with either $x > 0$, $x < 0$, $y > 0$ or $y < 0$) pierced by a total flux $\Phi = 1/2$, per period along z. The dashed line in (i) and (j) encloses a region with $\Phi = 1/2$. (k) and (l) show F_z in the planes $z = 0$ and $z = 0.5$, respectively. (m) magnetization in the (x, y) plane at $z = 0$, colored according to the HSL colormap shown in (d). (n) magnetization is plotted for the regions with $0.3 < |m_z| < 0.8$, at $z = 0$, highlighting the boundaries of the vortex region and antivortex regions, which are indicated by black dashed lines. All lengths are measured in units of the spiral period.

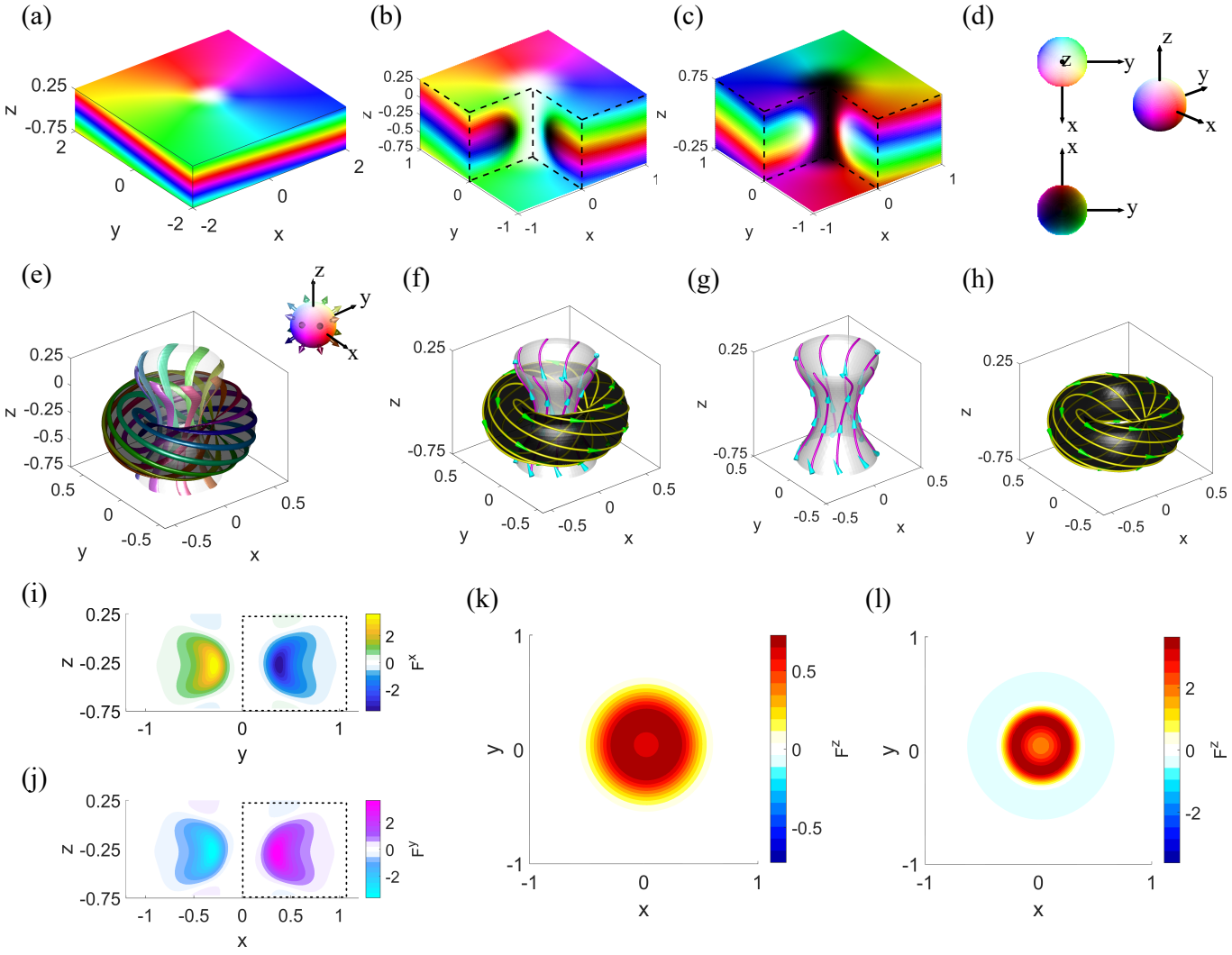

FIG. S9. Numerically relaxed magnetization configuration of the Twiston with $\nu = +1$ described by the asymptotic behavior $\phi = \nu\chi + qz$ for the far field. (a) displays a box of height L_{D}. The HSL colourmap shown in (d) is used to represent the magnetization direction $\mathbf{m}$ in panels (a) to (c). (b) and (c) show cuts through the centre of the box, for textures with $(N_{\mathrm{sk}}, H) = (p/2, 3/4)$ where $p = +1$ and $p = -1$ respectively, that are related simply by a transformation $\mathbf{m} \to -\mathbf{m}$. The texture illustrated in Fig. 4(f) corresponds to panel(c). Panel (e) shows selected preimages of magnetization for $m_z = \pm 0.5$, overlaid on the isosurfaces of $m_z = \pm 0.5$. (f) depicts the field lines of the emergent magnetic field $\mathbf{F}$, overlaid on the isosurfaces of $m_z = \pm 0.5$. (g) and (h) separately display the data from (f) for $m_z = +0.5$ and $m_z = -0.5$, respectively. (i) and (j) present plots of F_x and F_y, respectively, with each half-plane (with either $x > 0$, $x < 0$, $y > 0$ or $y < 0$) pierced by a total flux $\Phi = 1/2$, per period along z. The dashed line in (i) and (j) encloses a region with $\Phi = 1/2$. (k) and (l) show F_z in the planes $z = 0.25$ and $z = -0.25$, respectively. All lengths are measured in units of the spiral period.